

Progress on 3D Printed Loop Heat Pipes

Rohit Gupta¹, Chien-Hua Chen², and William G. Anderson³
Advanced Cooling Technologies, Inc., Lancaster, PA, 17601

The rapid growth of the miniaturized satellite industry has led to increased demand for low-cost and robust thermal management systems. Advanced Cooling Technologies, Inc. has been developing Loop Heat Pipes with 3D printed evaporators in an effort to reduce manufacturing costs and lead times by eliminating labor-intensive processes that are otherwise involved in the fabrication of standard evaporators. These processes include, but are not limited to, the primary wick fabrication, wick insertion, and knife-edge seal. The reported work describes the latest progress in this technology in the areas of primary wick advancement and thermal performance improvement. Following iterative optimization in this work, the pore size of the 3D printed wick was reduced to a sub-5-micron level, with a maximum radius of 4.9 μm . A new evaporator was 3D printed, featuring a refined primary wick and a fully-dense front wall, in order to prevent vapors from the vapor plenum being forced back into the evaporator under strong adverse pressure gradients. The overall thermal conductance of the system was improved by over 15% by incorporating a new saddle design with a single, connected structure and featuring a horizontal clamping mechanism. The new 3D printed evaporator assembly was also shown to operate successfully at a steady state power level of 350 W using line tubing with diameter of 0.003 m and ammonia as the working fluid.

Nomenclature

C	= thermal conductance (in $\text{W}/^\circ\text{C}$)
d	= outer diameter (in m)
l	= length (in m)
P	= power (in W)
p	= pressure (in Pa)
T	= temperature ($^\circ\text{C}$)
t	= time (in s or min)
r	= maximum pore radius (in μm)
w	= wall thickness (in m)
σ	= standard deviation
θ	= inclination angle (in degrees)

I. Introduction

Low-cost miniaturized satellites, in particular SmallSats and CubeSats, are being used increasingly for research, technology demonstrations, and commercial applications due to reduced costs and added capability for rapid deployment as compared to the full-scale counterparts. Given the meteoric rise in the use of this technology, there is an ever-growing demand for low-cost yet robust systems for thermal management and control. Loop Heat Pipes (LHPs) are commonly employed as thermal control systems on spacecraft due to the inherent thermal efficiency and design flexibility, allowing for the integration of the condensing region with deployable radiators. However, the fabrication of a standard LHP evaporator involves several labor-intensive processes, such as wick fabrication, wick insertion, vapor-groove fabrication, and the creation of a knife-edge seal, which is required to seal the pressure difference between the evaporator and the compensation chamber.¹ The high-costs associated with these processes render it unfeasible for cost-sensitive applications, such as for thermal management on miniaturized satellites. 3D

¹ R&D Engineer II, 1046 New Holland Avenue, Lancaster, PA 17601.

² Lead Engineer, 1046 New Holland Avenue, Lancaster, PA 17601.

³ Chief Engineer, 1046 New Holland Avenue, Lancaster, PA 17601.

printed LHP evaporators have been under development at Advanced Cooling Technologies, Inc. (ACT)^{2,3} in an effort to reduce system costs using Direct Metal Laser Sintering (DMLS). In DMLS, the desired metal part is fabricated in a layered sequence, following a 3D computer model. In most 3D printing applications, the powdered metal is melted in its entirety to create a fully-dense structure. For the current application, the DMLS parameters, such as the laser intensity, are programmed to vary during printing in order to produce bi-porous structures, with an inner porous region, without complete melting, surrounded by a fully-dense outer wall. This dichotomy in the porosity can be observed from magnified images of a DMLS sample presented in Figure 1. The porous region serves as the primary wick, providing sufficient capillary pressure to overcome the total pressure drop in the LHP during steady-state operation. In addition to the porous primary wick and the solid outer wall, several vapor grooves are also incorporated in the 3D model, leading to the fabrication of a full evaporator structure in a single process. Without the need for separate wick fabrication, wick insertion, and knife-edge seal, the 3D printed evaporators are estimated to provide over an order-of-magnitude savings in the manufacturing costs, making the technology attractive for use in emerging space applications.

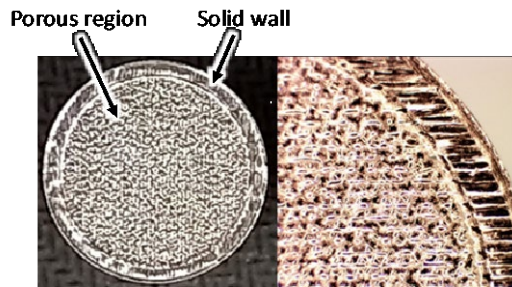


Figure 1 3D printed sample featuring an inner porous region surrounded by a solid outer wall.

Past developments on 3D printed evaporators at ACT have been detailed in two previous publications.^{2,3} A photograph of a 3D printed evaporator from a previous study along with a sectional view from a corresponding CAD rendering is presented in Figure 2. All of the evaporators from the previous and current efforts, which are discussed in this paper, are printed from 316L stainless steel metal powder and are associated with a length of $l = 0.1$ m and outer diameter of $d = 0.025$ m. The stainless steel construction of the primary wick is designed to minimize heat leak to the compensation chamber as compared to the Nickel wick construction of standard evaporators, which are associated with a higher thermal conductivity. The evaporator vapor grooves, designed to feed the vapor generated in the primary wick to the vapor line, can be identified clearly from Figure 2. As indicated previously, the vapor grooves are incorporated in the fabrication process, leveraging the unique capability of 3D printing to form cavities that are otherwise difficult to fabricate using conventional machining methods. However, a cap is welded around the front of the evaporator, which acts as a vapor plenum that feeds the collected vapor to the vapor line.

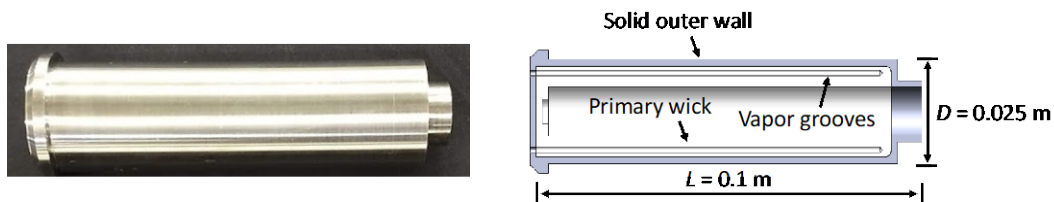


Figure 2. (left) A 3D printed LHP evaporator from a previous effort; (right) Evaporator sectional view from a corresponding CAD rendering.

A standard in-house LHP setup, shown in Figure 3, is used for thermal performance study of all 3D printed evaporators.^{2,3} The standardization of the LHP setup is necessary for accurate evaluation of the relative performance of evaporators that are printed following different sets of DMLS parameters. The dimensions of the vapor, condenser, and liquid lines for this LHP setup are listed in Table 1. An image of the full LHP setup indicating all of the major components is presented in Figure 3. Besides proof-of-concept demonstrations, previous efforts were successful at advancing the capillary limit of 3D printed evaporators through pore size minimization, leading to an increase in the

dryout power limit from an initial $P \approx 50$ W to $P = 125$ W with ammonia as the working fluid. The conductance of the system was also elevated to $C = 6.2$ W/°C from an initial $C = 2.8$ W/°C using a combination of firm clamping and thermal grease for improved thermal contact between the saddle and the evaporator. Beyond the previous work, the current program is aimed at further advancement of the primary wick and improvement of the LHP thermal characteristics with the overarching goal of achieving performance parity with standard LHPs. The results of the current program are presented in the following section.

Table 1 Dimensions of various components in the standard ACT LHP architecture

Component	Length, l (m)	Outer diameter, d (m)	Wall thickness, w (m)
Vapor line	0.20	3.18×10^{-3}	5×10^{-4}
Condenser	3.35	3.18×10^{-3}	5×10^{-4}
Liquid line	0.40	3.18×10^{-3}	5×10^{-4}
Compensation chamber	0.10	0.03	16.5×10^{-4}

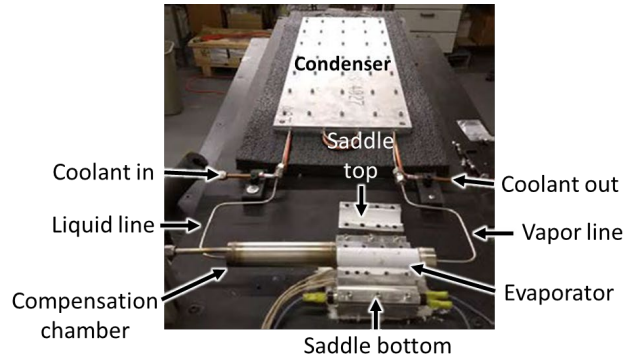


Figure 3. Standard LHP setup used for testing of 3D printed evaporators at ACT.

II. Results

A. Advancement of 3D Printed Primary Wick

Efforts at reducing the maximum pore size associated with a contiguous path in the primary wick were undertaken with the ambitious goal of achieving a radius of $r = 1\text{-}2$ μm that is characteristic of furnace-sintered wicks. An iterative process was employed to drive the optimization of the DMLS parameters for better capillary performance. In the first step, a cylindrical wick sample, see Figure 4, was printed with a diameter of $d = 0.01$ m and length of $l = 0.03$ m using an initial set of DMLS parameters. The maximum pore radius of the fabricated sample was measured using a bubble point test following the ASTM E128 standards.⁴ As part of this test, a known pressure was applied to one end of a sample from a compressed nitrogen source, whilst the other end was kept at fixed atmospheric pressure. The sample was placed just below the methanol free surface and kept submerged for the entire duration of the test. The applied pressure was gradually increased until the emergence of a dynamic bubble column from the sample free end, indicating a breach in the capillary limit associated with the wick.



Figure 4. 3D printed wick sample used in the current study for the advancement of primary wick.

Care was taken to ensure “wetting” in the sample bulk in order to eliminate potential edge irregularities at the free surface from contaminating the test results. The measured pore size was recorded before proceeding to the next step of the iteration wherein a new wick sample, with identical dimensions as the previous sample, was attempted following a new set of DMLS parameters with the goal of improving upon the capillary limit over the previous step of the iteration. A total of four cylindrical samples were printed during the current reporting period, representing four iteration steps. Each of these samples was fabricated from 316L stainless steel metal powder to ensure measurement consistency between the samples and potential full-scale evaporators.

A timeline of wick advancement is presented in Figure 5. From Figure 5, the optimization routine was successful in reducing the pore size at each step of the iteration, with the maximum pore radius of Sample 4 measured to be over 40% smaller than the radius of Sample 1. The maximum pore radii associated with each of the four samples is listed in Table 2 below. It should be highlighted that Sample 4 represents the first instance of a sub-5-micron DMLS wick that has been achieved in the 3D printed LHP program at ACT, denoting a significant improvement over the $r \approx 44 \mu\text{m}$ wick² from the very first attempt at DMLS wick fabrication. It is also important to note that the 40% reduction in pore radius in the current effort corresponds to over 20% increase in the LHP power limit for Sample 4 over Sample 1, as estimated using an in-house power limit calculator.

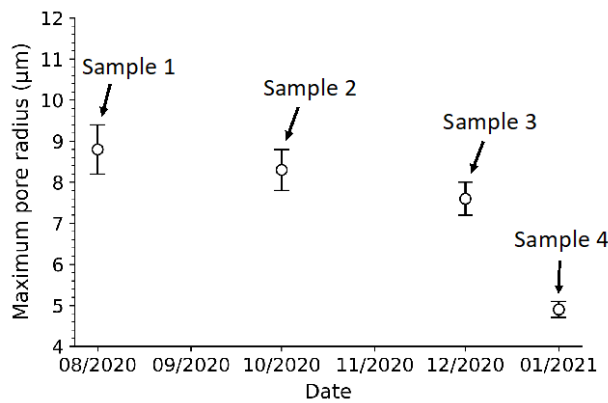


Figure 5. Timeline of pore size reduction of 3D printed primary wick in the current program.

The error bars in Figure 5 and the uncertainty values in Table 2 span a 1- σ confidence interval, providing a measure of the scatter in the 3D printing process from bubble test measurements conducted on several copies of a given sample, corresponding to an identical set of DMLS parameters. The copy-to-copy variation in the pore radii for each of the four samples was measured below a $\sigma = 1 \mu\text{m}$ level within a 68% confidence interval, indicating a high degree of repeatability in the 3D printing process. It should also be highlighted that the bubble point tests were repeated in a bath of IPA and the acquired measurements were found to be consistent with those reported above using methanol, establishing additional confidence in the measurement process.

Table 2. Maximum pore radii measurements for 3D printed wick samples from the current program

<u>Sample</u>	<u>Max. pore radius (in μm)</u>
Sample 1	8.8 ± 0.6
Sample 2	8.3 ± 0.5
Sample 3	7.6 ± 0.4
Sample 4	4.9 ± 0.2

As a secondary objective in primary wick advancement, the DMLS fabrication of an additional high-porous sample was attempted, with porosity near 50%, motivated by the goal of maximizing wick permeability and consequently minimizing the pressure drop in the primary wick during LHP operation. The printed sample, referred to here as Sample 5, with identical dimensions as Samples 1–4, was measured to have a porosity of 49%, providing a significant increase over the sub 30% porosities of the other four samples. For a more direct characterization, measurements of the permeability were acquired for each of the samples using an in-house permeability apparatus. This apparatus features a U-shaped design with uniform cross section. As part of this U-shape, two vertically-oriented cylindrical

tubes are connected at the base with a horizontal arm. The horizontal arm in turn, contains a small gap in the center to allow for the installation of the cylindrical wick sample, providing a connected path for the flow of methanol, which was used as the working fluid. At the start of the experiment, the vertical tubes were filled with methanol to different heights prescribed by the desired initial pressure difference across the installed sample. Driven by the imposed pressure gradient, the difference in the methanol column was observed to gradually diminish over time. After a set time interval, the height difference was recorded once again, indicating the end of the experiment. The wick permeabilities were then calculated from the acquired initial and final height differences using an integrated form of Darcy’s law. For comparison, the permeabilities of Sample 2 and Sample 5 are presented in Table 3.

Table 3. Permeabilities for select 3D printed wick samples from the current study

Sample	Porosity	Permeability ($\times 10^{-13} \text{ m}^2$)
Sample 2	29%	1.16 ± 0.05
Sample 5	49%	11.7 ± 0.5

From Table 3, an increase in porosity by a value of 20% is associated with an order-of-magnitude increase in the wick permeability, demonstrating a significant co-dependence between these variables. However, this improved permeability is expected to cause a significant drop in the capillary limit owing to a distinct increase in the maximum pore size from $r = 8.3 \pm 0.5 \mu\text{m}$ for Sample 2 to $r \approx 27 \mu\text{m}$ for Sample 5. The power limits for Sample 2 and Sample 5, estimated using the ACT analytical power calculator, are presented in Table 4. The maximum pore radii for these samples are also included in Table 4, for reference. From Table 4, Sample 2 is associated with a significantly higher power capacity as compared to Sample 5. Thus, while the improved permeability for Sample 5 contributes to reduced flow resistance in the primary wick, the contributions to the net resistance of the standard ACT LHP setup stem primarily from the vapor line and the condenser. With a significantly diminished capillary limit and with only a marginal improvement in the LHP resistance, the power transport capacity for Sample 5 is greatly disrupted, with a predicted 48% decline as compared to Sample 2.

Table 4. Analytical power limit for select 3D printed wick samples from the current study

Sample	Max. pore radius (μm)	Power limit (W)
Sample 2	8.3 ± 0.5	340
Sample 5	~ 27	175

A comparison between the pore-perm properties of furnace-sintered wicks and DMLS wicks is presented in Figure 6. The solid line in Figure 6, called the Anderson curve, describes a linear fit through the pore-perm data points for a large array of furnace-sintered wicks that have been manufactured at ACT.³ Sample 2 and Sample 5 from the current set of DMLS wicks are presented as solid markers in Figure 6. From Figure 6, the DMLS samples are associated with reduced permeability as compared to furnace-sintered wicks, for a given pore size. However, the capacity to print high-porous wicks, as demonstrated with Sample 5, can be leveraged in the future to develop advanced bi-porous wick structures with a high-porous inner region surrounded by a thin annular region with high capillary limit, thereby driving the performance envelope closer to furnace-sintered wicks from Figure 6.

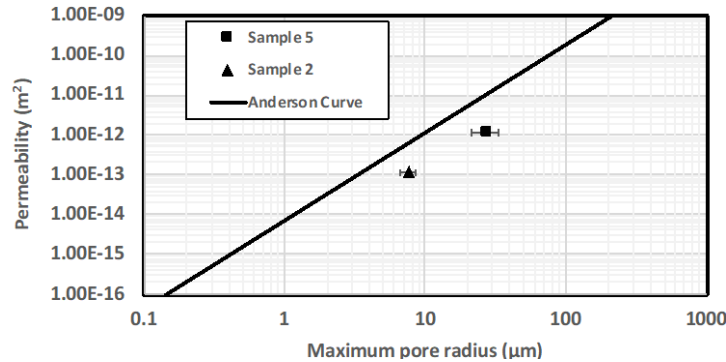


Figure 6. Pore-perm comparison between the 3D printed wicks from the current program and the furnace sintered wicks at ACT, which is described by the solid trend line.

For a final task in wick advancement, Sample 5 was also subjected to Hot Isostatic Pressing (HIP) in order to evaluate HIP effectiveness for potential future use to provide additional compression, beyond DMLS, that may be needed to achieve the desired pore size of $r = 1\text{-}2\ \mu\text{m}$. As part of HIP, the wick sample was subjected to an isotropic, high-pressure and high-temperature environment with $p = 1.03 \times 10^8\ \text{Pa}$ and $T = 1163 \pm 14\ \text{°C}$, and for an extended time period of $t = 240 \pm 15\ \text{min}$.⁵ The HIP-based compression was found to very effective, causing a reduction in pore size by over 18% from $r \approx 27\ \mu\text{m}$ to $r \approx 22\ \mu\text{m}$.

B. Thermal Performance Improvement of 3D Printed LHP

During the wick advancement study, the DMLS parameters for Sample 3 were selected to form the primary wick for a new full-scale evaporator for thermal performance comparison with LHP from previous studies. Besides an advanced wick, the new evaporator also featured a fully-dense front wall as opposed to the porous front end of the old evaporators. The solid front wall was incorporated in the latest design to prevent, with complete certainty, any potential leakage of vapor from the vapor plenum back into the evaporator under strong adverse pressure gradients. A photograph showing a comparison of the old and the new evaporator front ends is presented in Figure 7.

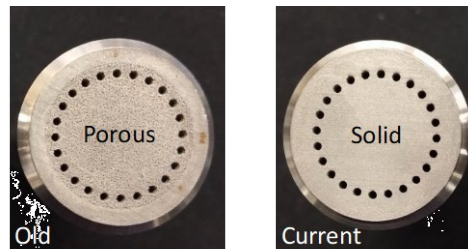


Figure 7. A comparison of the porous front end of evaporators from the previous programs with the solid front end from the current program.

Besides the aforementioned changes, however, the new evaporator was printed identical to those used in the past. As indicated previously, the standard ACT LHP setup was used yet again for the performance study with ammonia as the working fluid. Before testing, however, a measurement of the pore size at bubble point was acquired for the full-scale evaporator and found to be equal to the $r \approx 7.6\ \mu\text{m}$ pore size for Sample 3, indicating scaling consistency of the DMLS process. It should be noted that in the ACT LHP setup, the evaporator is installed in an aluminum saddle, which in previous studies was designed to have separate top and bottom sections, see Figure 8 (*left*), that clamped around the evaporator using a series of vertically-oriented fasteners. A noticeable temperature difference of $\Delta T \approx 8\ \text{°C}$ was observed between the two sections during operation at moderate-to-high power input, limiting the overall conductance of the LHP to $C = 6.2\ \text{W/°C}$ at a point-of-comparison power input of $P = 160\ \text{W}$. In a standard LHP evaporator installation, the furnace-sintered primary wick connects with the saddle through an interference fit, thereby minimizing the thermal resistance at the region of contact. However, due to a concerted effort at minimizing labor-intensive processes in LHP manufacturing, a simple compression fit along with an application of thermal grease was employed for connecting the 3D printed evaporator with the saddle.

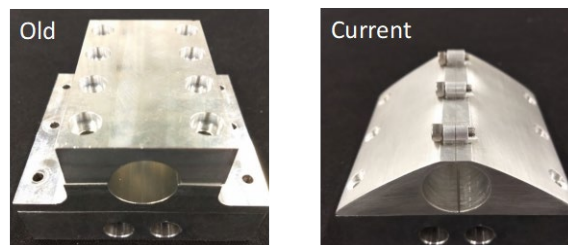


Figure 8. A comparison of the old evaporator saddle from the previous program with the saddle from the current program.

Despite firm campling, the two-part saddle design from Figure 8 (*left*) allows for a tiny air gap that is sandwiched between the top and bottom sections, which expands at the higher temperatures and inhibits heat flow across this region contributing to the elevated temperature difference and reduced conductance. In order to address this problem, a new saddle was designed which eliminates the air gap problem of the previous saddle by incorporating a single, unified structure with a horizontal clamping mechanism, as seen in Figure 8 (*right*). This new saddle was also fabricated out of aluminum and featured a layer of thermal grease for improved contact with the evaporator. With LHP operation at an identical steady-state power input of $P = 160$ W, the saddle temperature difference was observed to drop to a level of $\Delta T \approx 5$ °C, thereby elevating the overall conductance of the LHP to $C = 7.3$ W/°C.

Select temperature profiles acquired during LHP operation with ammonia, featuring the new evaporator and saddle, are presented in Figure 9.

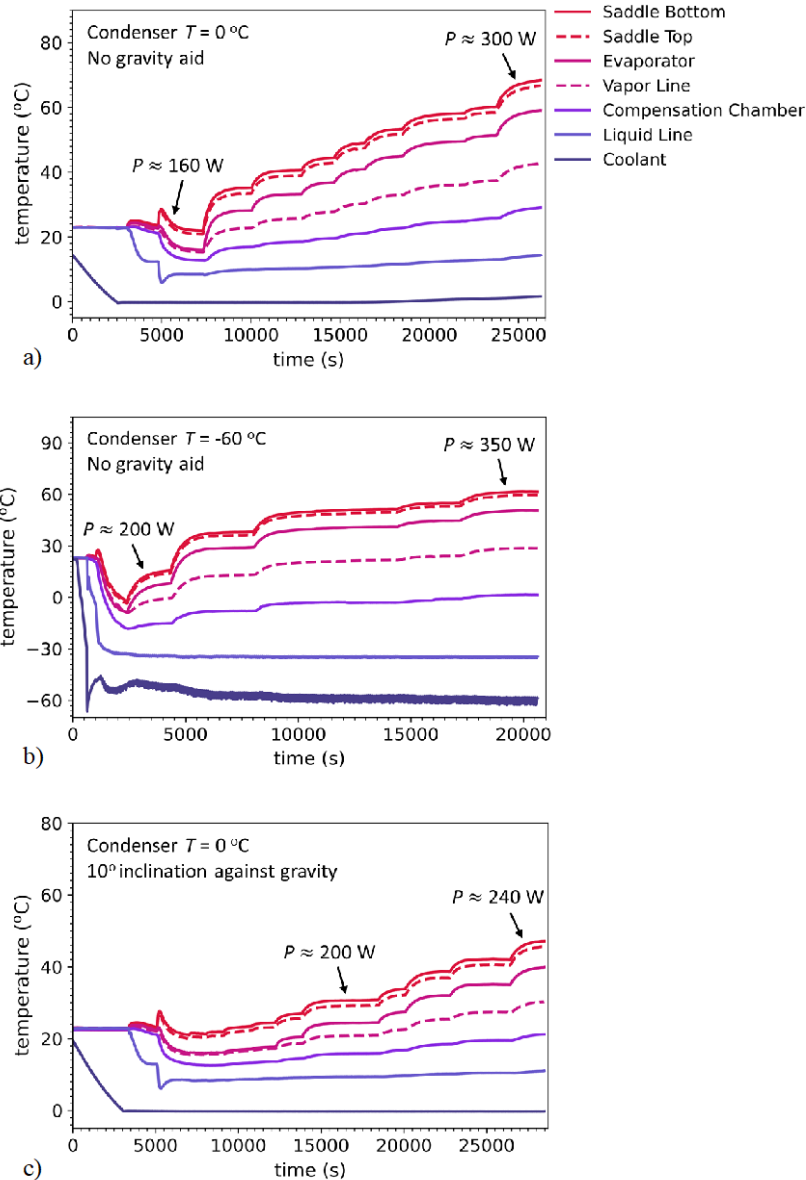


Figure 9. Temperature profiles for LHP operation with new evaporator and saddle at two different condenser temperatures ($T = 0$ °C, -60 °C) and system orientations ($\theta = 0^\circ$, 10°) with ammonia as the working fluid.

Figure 9 a) and b) correspond to non-gravity aided LHP operation at two different condenser temperatures of $T = 0\text{ }^{\circ}\text{C}$ and $T = -60\text{ }^{\circ}\text{C}$, respectively. The temperatures in Figure 9 c) were, in contrast, acquired during LHP operation in reflux mode, with the evaporator raised relative to the condenser to provide an effective system orientation of $\theta = 10^{\circ}$, with horizontal. Given significant interest in thermal management and control for lunar missions, the selected angle intends to simulate a vertically-oriented LHP operation against gravity on the lunar surface.

Without gravity aid, the new evaporator proved capable of successfully operating at input powers of $P = 300\text{ W}$ and $P = 350\text{ W}$ at condenser temperatures of $T = 0\text{ }^{\circ}\text{C}$ and $T = -60\text{ }^{\circ}\text{C}$, respectively, demonstrating significant improvement over the dryout power limit of $P = 125\text{ W}$ of the old evaporator. Even when oriented against gravity, the current system was operated successfully at a steady-state power of $P = 240\text{ W}$. It is important to note that the reported power levels are comfortably within the capillary limit of the new LHP evaporator. As an example, using the ACT power calculator, the steady-state power at capillary limit in horizontal operation, for a condenser temperature of $T = 0\text{ }^{\circ}\text{C}$, is expected to be around $P = 350\text{ W}$, which is markedly greater than the demonstrated operation at $P = 300\text{ W}$. The LHP, in the current study, was operated conservatively from an abundance of caution that stems from testing of a new installation. The variation in thermal conductance with power, for the operational case from Figure 9 a), is presented in Figure 10.

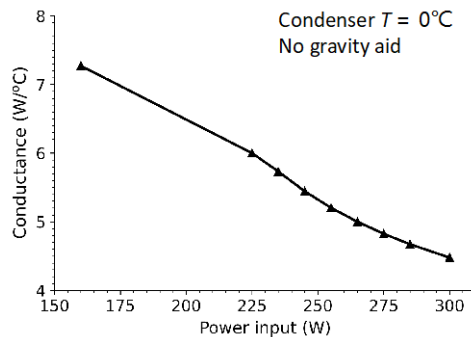


Figure 10. Conductance variation of the LHP with new evaporator and saddle as a function of power input for condenser $T = 0\text{ }^{\circ}\text{C}$ and without gravity aid.

The overall system conductance is observed from Figure 10 to decrease with increasing input power. While not shown here for brevity, the conductance values are also largely similar to the LHP operation at an orientation of $\theta = 10^{\circ}$ against gravity. It is interesting to note that the 3D printed LHP of the current program has a higher conductance than the standard ACT LHPs, from internal reports, at input power below $P = 200\text{ W}$. The better conductance for the 3D printed system can be attributed to the low thermal conductivity of the stainless steel primary wick in the DMLS evaporator as opposed to Nickel wicks in the standard LHPs, which are associated with greater heat leakage to the compensation chamber during operation. With increasing operating power, however, the conductance of the 3D printed LHP drops rapidly and falls below the level of the standard LHP, driven primarily by the elevated temperature difference between the evaporator and the vapor line, as seen in Figure 9 a). As part of future work, the overall thermal conductance of the system will be improved by exploring advanced vapor groove designs to provide a high surface area for vaporization. Moreover, beyond the primary wick, the secondary wick will also be fabricated using DMLS, which will further minimize the manufacturing cost of the LHP.

III. Conclusion

The advancement of primary wick and the improvement in thermal performance of 3D printed evaporators are detailed in this paper. An iterative optimization of DMLS parameters was successful in reducing the maximum pore size of the primary wick down to $r \approx 4.9\text{ }\mu\text{m}$, documenting the first instance of a sub-5-micron DMLS wick at ACT. As proof-of-concept, a high-porous wick, with porosity of 49%, was also fabricated successfully using DMLS. This exercise in porosity control was crucial for future development of advanced, bi-porous wicks that combine the high capillary limit of a “fine” wick with low flow resistance offered by a “coarse” wick. A new 3D printed evaporator, with a primary wick pore size of $r \approx 7.6\text{ }\mu\text{m}$, was also fabricated in the current program. This evaporator featured a solid front end to prevent any vapor push-back from the plenum under strong adverse pressure gradients. Using a redesigned saddle featuring a single, connected structure, the new LHP evaporator was shown to operate comfortably

at an input power of $P = 350$ W at the lowest condenser temperature, demonstrating significant improvement as compared to the dryout power limit of $P = 135$ W of the older DMLS evaporators. Moreover, due to the new saddle, the overall conductance of the system was seen to improve from $C = 6.2$ W/°C to $C = 7.3$ W/°C at $P = 160$ W. Future work will be split between continued enhancement of thermal performance of the LHP through the use of advanced vapor groove designs and the fabrication of DMLS secondary wicks for further minimization of the LHP manufacturing costs.

Acknowledgments

This work was funded by NASA through the Small Business Innovation Research (SBIR) program under contract 80NSSC20C0271. The technical monitor is Ms. Stephanie Mauro.

References

- ¹ Anderson, W.G., Dussinger, P.M., Garner, S.D., Hartenstine, J.R., and Sarraf, D.B., "Loop Heat Pipe Design, Manufacturing, and Testing – An Industrial Perspective," *ASME Heat Transfer Summer Conference*, San Francisco, California, 2009.
- ² Richard, B., Pellicone, D., and Anderson, W.G., "Loop Heat Pipe Wick Fabrication via Additive Manufacturing," *48th International Conference on Environmental Systems*, Albuquerque, New Mexico, 2018.
- ³ Richard, B., Anderson, W., Chen, C.-H., Crawmer, J., and Augustine, M., "Development of a 3D Printed Loop Heat Pipe," *49th International Conference on Environmental Systems*, Boston, Massachusetts, 2019.
- ⁴ ASTM E128-99, "Standard Test Method for Maximum Pore Diameter and Permeability of Rigid Porous Filters for Laboratory Use," *ASTM International*, West Conshohocken, Pennsylvania, 2019.
- ⁵ Essa, K., Jamshidi, P., Zou, J., Attallah, M., and Hassanin, H., "Porosity Control in 316L Stainless Steel using Cold and Hot Isostatic Pressing," *Materials and Design*, 2018, pp. 21-29